Title: A scalable microstructure photonic coating fabricated by roll-to-roll "defects" for daytime sub-ambient passive radiative cooling

Authors: Sipan Liu[1†], Chenxi Sui[2,3†], Myers Harbinson[1], Michael Pudlo[1], Himendra Perera[4], Zhenzhen Zhang[5], Ruguan Liu[6], Zahyun Ku[7], Md Didarul Islam[1], Yuxuan Liu[1], Yong Zhu[1], Jan Genzer[4], Saad Khan[4], Po-Chun Hsu[2,3*], Jong Eun Ryu[1*].

†These authors contributed equally to this work.

*Corresponding author. Email: pochunhsu@uchicago.edu (P. Hsu); jryu@ncsu.edu (J. Ryu).

Affiliation:

1. Department of Mechanical and Aerospace Engineering, NC State University, Raleigh, NC, USA
2. Pritzker School of Molecular Engineering, University of Chicago, Chicago, IL, USA
3. Department of Mechanical Engineering and Materials Science, Duke University, Durham, NC, USA
4. Department of Chemical and Biomolecular Engineering, NC State University, Raleigh, NC, USA
5. Revibe Technologies, Wake Forest, NC, USA
6. Robotics department, Amazon, Inc, Westborough, MA, US
7. Materials and Manufacturing Directorate, Air Force Research Laboratory, WPAFB, OH, USA

Abstract

The deep space's coldness (~4K) provides a ubiquitous and inexhaustible thermodynamic resource to suppress the cooling energy consumption. However, it is nontrivial to achieve sub-ambient radiative cooling during daytime under strong direct sunlight, which requires rational and delicate photonic design for simultaneous high solar reflectivity (> 94%) and thermal emissivity. A great challenge arises when trying to meet such strict photonic microstructure requirements while maintaining manufacturing scalability. Herein, we demonstrate a rapid, low-cost, template-free roll-to-roll method to fabricate spike microstructured photonic nanocomposite coatings with Al_2O_3 and TiO_2 nanoparticles embedded that possess 97.5% of solar reflectivity and 98.6% of thermal emissivity. A novel Roll-to-roll Defects Coefficient is proposed to predict the microstructure density. When facing direct sunlight at summer noon (806 W/m^2 solar intensity), the meta-coatings show a radiative cooling power of 99.2 W/m^2. Combined with the coatings' superhydrophobic and contamination resistance merits, the potential 15.1% cooling energy saving capability is numerically demonstrated across the United States.

Keywords: Sub-ambient daytime cooling, Passive radiative cooling, Scalable photonic structure, Roll-to-roll fabrication

Climate change has severely impacted people's lives and the environment. Due to the rising temperature, approximately 14% of primary energy was used in the building cooling system in the US [1,2], presenting a challenge towards a sustainable future. Passive radiative cooling (PRC) materials are innovated to mitigate cooling consumption by delivering wireless access to the cold thermodynamic resources (~4K) in deep space [3–12]. By reflecting solar radiation and radiating heat into the cold universe through the atmospheric transparent window,

the radiative cooling materials can achieve noticeable cooling energy saving under the direct sunlight. The ideal radiative cooling materials should simultaneously possess high cooling power, low-cost, scalable manufacturing, and contamination resistance characteristics. Previous research showed that spike photonic microstructures could achieve high cooling power and anti-contamination at the same time [3,13], since the rough surfaces elevated the thermal emissivity by creating a gradually refractive index change and generating a superhydrophobic surface [3]. However, nontriviality arises when fabricating the desired microstructures with low-cost and scalability because high mid-infrared (mid-IR) emissivity needs high-precision control of the photonic microstructures, where costly and low-yield nanofabrication techniques are generally considered [3,13]. Thus, innovative manufacturing methods need to be developed to fabricate these microstructures for large-scale applications, such as building energy saving.

The common ribbon and spike defects in traditional roll-to-roll manufacturing inspired researchers to develop a novel scalable way to fabricate periodical microstructures [14–17]. Specifically, the positive pressure gradient generated in the downstream meniscus sows the seeds of the spike "defects" on the surface [18–20]. These defects can be robustly kept when the material's rheological properties are modified by adding nanoparticles. In this situation, the defects' peak periodicity is correlated with material properties (i.e., surface energy, viscosity) and fabrication parameters (i.e., roller radius, roller gap, and roller speed) [21–23]. By manipulating the embedded nanoparticles and fabrication parameters, the optimized spike microstructures for high cooling performance can be obtained. In addition, metal oxide nanoparticles are able to reflect sunlight due to the particles' backscattering [24–26], which potentially further enhances the daytime radiative cooling power. Therefore, the modified roll-to-roll manufacturing method could be a cost-effective candidate for fabricating high-performance daytime radiative cooling photonic structures on a large scale.

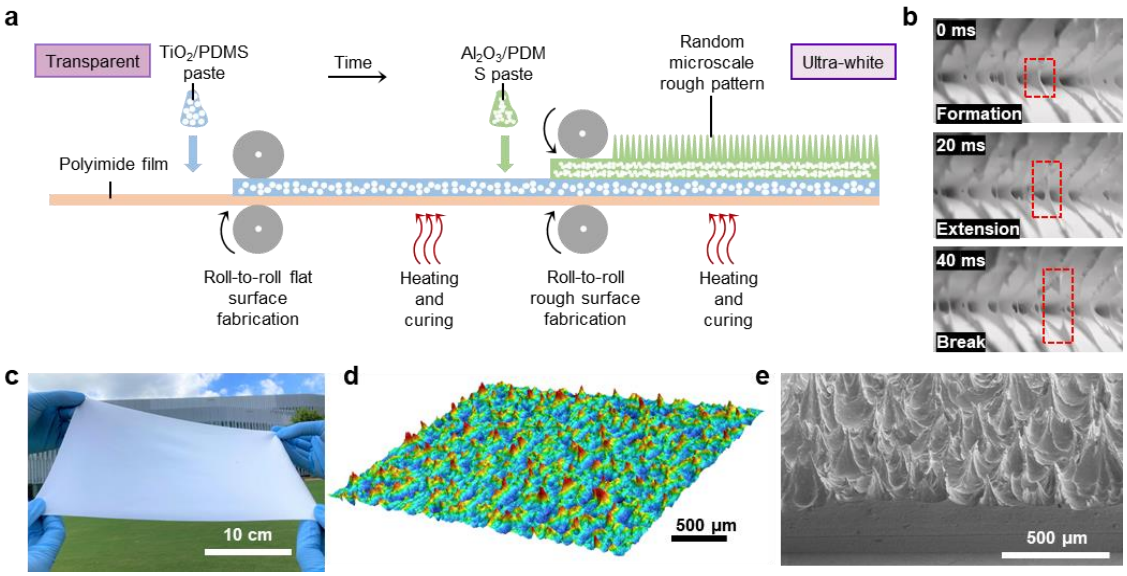

Fig. 1. (a) Schematic of the bilayer nanocomposite microstructure photonic coating fabrication. (b) The formation of the spike on the photonic coating during the roll-to-roll fabrication process. (c) The photonic coating photograph. (d) Laser confocal picture of the photonic coating surface. (e) SEM picture of the photonic coating with a cross-section view.

Inspired by previous work, we demonstrate a template-free roll-to-roll method combined with polymetric nanocomposites to fabricate spike photonic coatings for daytime radiative cooling (Fig. 1(a-e) and Supplementary information (SI) Fig. S1-S2). A novel bilayer structure (Al_2O_3/polydimethylsiloxane (PDMS) and TiO_2/PDMS) is employed to enhance the reflectivity of ultraviolet (UV) and visible (Vis) light separately (Fig. 2(a)). The as-fabricated materials (photonic coatings) show an emittance in mid-IR of 98.6% and a state-of-the-art substrate-independent solar radiation reflectance of 97.5% (Fig. 2(b)). The photonic coating generates a sub-ambient cooling power as high as 99.2 W/m^2 in the daytime, and the building energy modeling result showed 15.1 % cooling system energy (33.4 GJ/year) across the US. By comparing with the state-of-the-art radiative cooling materials (Fig. 2(c), S.I.2-3, normalized in the ASTM G173-03 Reference Global Tilt Solar Spectra and atmospheric transparent window of Durham, NC, USA), our photonics coating has a high solar reflectivity, thermal emissivity, and thus cooling power[3–9]. Besides, the photonic coating possesses superhydrophobic merit (water contact angle = 156º) which promotes resistance to contamination (Fig. 2(d) and S.I.4).

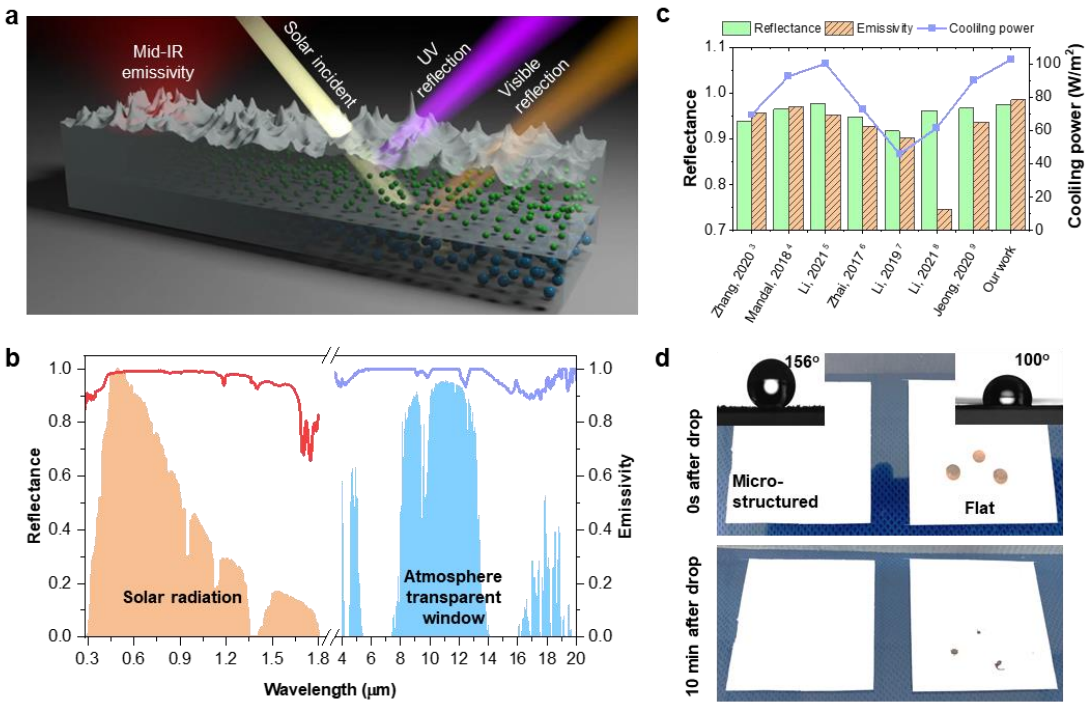

Fig. 2. (a) The schematic of the bilayer photonic coating passive radiative cooling, including mid-IR emittance and separately governing the UV. The smaller green spheres are Al_2O_3, larger blue spheres are TiO_2. (b) Spectral reflectance and emissivity of the photonics coating (bilayer, thickness is 300 μm) presenting against normalized ASTM G173-03 Reference Global Tilt Solar Spectra and mid-IR transparent window of Durham, NC, USA. (c) Comparing the solar reflectance, emissivity, and theoretical cooling power (normalized in the same ASTM G173-03 Reference Global Tilt Solar Spectra and weather condition of Durham, NC, USA.) with the state-of-the-art radiative cooling materials record in the reference[3-9]. (d) Photonic coating's superhydrophobicity (water contact angle = 156º) and contamination resistance demonstration with 30 º slope (Side view picture was in Fig. S3).

Results

Design of the photonic coating materials

As mentioned above, the ideal radiative cooling materials should possess high solar reflectivity and thermal

emissivity. To achieve this goal, the visibly transparent PDMS is used for a high thermal emission. To enhance solar reflectivity, the TiO_2 and Al_2O_3 nanoparticles are mixed with PDMS. TiO_2 is a commercialized white painting material that can have high reflectivity with a thin thickness due to its high refractive index (~2.7). However, the TiO_2 highly absorbs the UV and blue light due to the 3.0 eV bandgap (413 nm), which limits the solar reflectivity below 91% [27]. To tackle this challenge, low-cost Al_2O_3 nanoparticle is introduced to suppress the UV absorptivity. The final design of the bilayer photonic materials is shown in Fig. 1(a) and 2(a). The Al_2O_3/PDMS is layered on top of the TiO_2/PDMS to prevent the UV absorption of TiO_2. Theoretically, higher backscattering coefficients of the nanoparticles lead to higher reflectivity. To achieve maximum reflectivity, the backscattering coefficients of the nanoparticles were calculated by Mie's theory (Fig. 3 (a-b), S.I.5-6). 500 nm TiO_2 was chosen as it has a strong backscattering coefficient peak at the peak of solar radiation (500 nm), and 200 nm Al_2O_3 was chosen due to its high backscattering coefficient in the UV range and better processability in PDMS than 100 nm Al_2O_3 particles.

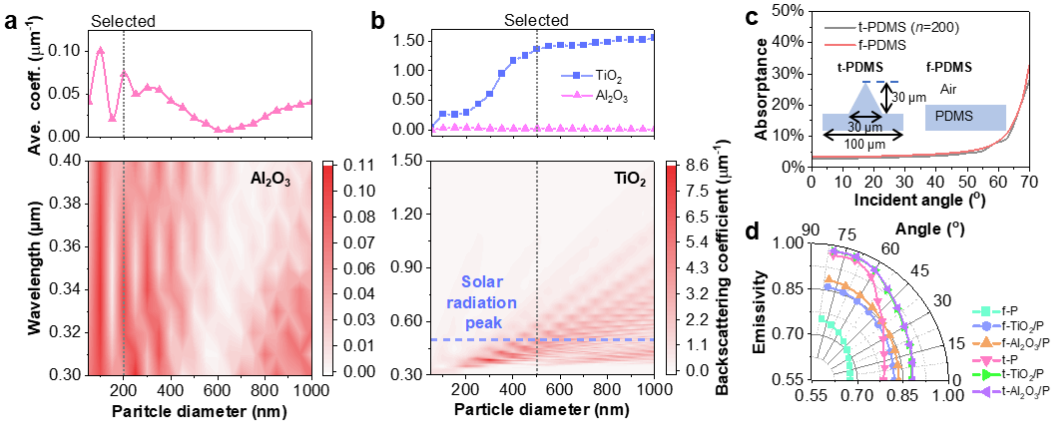

Fig. 3. (a-d) The nanoparticle/PDMS backscattering coefficients calculation by Mie's theory (particles concentrations were 25 vol%), (a) the Al_2O_3 nanoparticles' average backscattering coefficient, and the backscattering coefficient along the change of the particle diameter and wavelength at UV range, (b) the TiO_2 nanoparticles' average backscattering coefficient, and the backscattering coefficient along the change of the particle diameter and wavelength at solar spectra range. (c) The spike microstructure's effect on solar spectral reflectance, and the models in the RWAC model. In the legend, t- is a triangular spike model, f- is the flat model. (d) The enhancement results for the mid-IR emissivity by the photonic microstructures simulated by finite elements analysis (FEA, COMSOL, particles concentration was 25 vol%. In the legend, P is PDMS.

Besides the improved solar reflectivity, we further managed to elevate the thermal emissivity by fabricating the spike microstructures on the top surface of the coating. We found that the spike microstructures (~30 μm) only had a negligible effect on the solar spectrum reflectivity by Rigorous Coupled-Wave Analysis (RCWA) in Fig. 3(c), because of the huge mismatch between the wavelength of the incident light and the structure size (Fig. 3(c) and S.I.7). The spike microstructures could create a gradually refractive index change at the interface of the air and the coating, which enhanced the thermal emissivity [3]. The enhancement of the thermal emissivity by the photonic microstructures was simulated by finite element analysis (FEA, COMSOL Multiphysics 5.5, S.I.8). The FEA demonstrated that the microstructures significantly increase the hemisphere emissivity from 70.8% (flat PDMS, f-P) to 87.0% (triangular microstructured PDMS, t-P) at mid-IR (Fig. 3(d), S.I.7). The triangular microstructure also showed higher emissivity than square and circular topography (Fig. S9-S10). Boosted by the

strong mid-IR absorption of Al_2O_3 or TiO_2 nanoparticles (25 vol% particle concentration), the emissivity can be promoted further to 92.9% (Fig. 3(d) and Fig. S11). The simulation results also reveal that higher height and lower peak periodicity (denser) of the spike lead to a higher emissivity (Fig. S12), which guided our following roll-to-roll fabrication.

Materials' Fabrication and optical characterization

For cooling energy-saving applications, the radiative cooling photonic coating materials must be fabricated on a large scale. The rapid roll-to-roll method is used to fabricate TiO_2/PDMS and Al_2O_3/PDMS bilayer photonic coating materials with spike microstructures by employing viscoelastic fluid instability. The formation of the spike peaks is described in Fig. 1(b) and Video (for presenting convenience, 15 vol% Al_2O_3/PDMS (relative low viscosity) and low roller speed are utilized). Our previous simulation research demonstrated that surface energy γ, viscosity η, roller radius R, roller gap d, and roller speed U had strong correlations with the pressure gradient in the flow direction, which directly led to the formation of the spike "defects" [20]. To demonstrate the effects of η, U, γ, and R/d on the final spikes' peak periodicity (p_{spike}), parametric experiments are conducted with U ranging from 20 rpm to 100 rpm, and R/d from 100 to 320. The 4 - 24 vol% Al_2O_3/PDMS nanocomposites are prepared for different viscosities. The η *and* γ measurement results of the nanocomposites are shown in Fig. 4(a-b) and S.I.9. The parametric roll-to-roll experiment results demonstrate that the higher η (higher particle content), U and R/d would lead to smaller p_{spike} as shown in Fig. 4(c) and Table S4. Here, due to the Capillary number ($Ca=\eta U/\gamma$, used to be the index for predicting critical point of the roll-to-roll defect appearance, but the fabrication in this study is far beyond the critical point) could not fit the viscoelastic fluid's fabrication very well (Fig. S15), we propose a novel dimensionless Roll-to-roll Defects Coefficient, $RDC= ((\eta/\gamma)^{1/3}UR / d)^{-0.5}$, to fit with the p_{spike}. The p_{spike} *vs.* RDC result is shown in Fig. 4(d). A logarithmic proportion shows that the p_{spike} decreased as the RDC decreased. In the final bilayer products, a flat 25 vol% TiO_2/PDMS is first roll-to-roll fabricated and cured. Then, the top layer is fabricated on the flat layer by roll-to-roll method, where the 26 vol% Al_2O_3 and 3 vol% SiO_2 (10 nm, stabilization particles) are mixed into PDMS to achieve close-boundary viscosity but with processability. When the U went to 100 rpm and the R/d went to 320, the ~100 μm p_{spike} is achieved (Fig. 1(d-e)), which is desired for improving thermal emissivity (Fig. 1(d-e)).

To prove the radiative cooling capability of the photonic coating, it is necessary to characterize the optical properties of solar and mid-IR ranges. The ultraviolet-visible (UV-vis) and Fourier transform infrared (FTIR) spectrometers are used to characterize solar reflectivity and the mid-IR thermal emissivity, respectively. In Fig. 4(e), the UV-vis results show that the bilayer Al_2O_3/PDMS-TiO_2/PDMS coating overcomes the drawbacks of the Al_2O_3/PDMS (low overall reflectivity, 89.5%) and TiO_2/PDMS (high absorption at UV). A state-of-the-art 97.5% solar energy reflectance is achieved, which is comparable with PDMS/silver[28]. The FTIR measurement verified that the spike structure enhanced the mid-IR emission (Fig. 4(f)). A 98.6% emissivity is obtained from the structured bilayer Al_2O_3/PDMS-TiO_2/PDMS and the structured TiO_2/PDMS samples. The referenced materials, flat TiO_2/PDMS and flat PDMS, only achieve 93.5% and 89.0% emissivity, respectively. Such prominent optical properties of the photonic coatings guarantee a potential theoretical daytime radiative cooling performance of 102.9 W/m^2 (S.I.2-3).

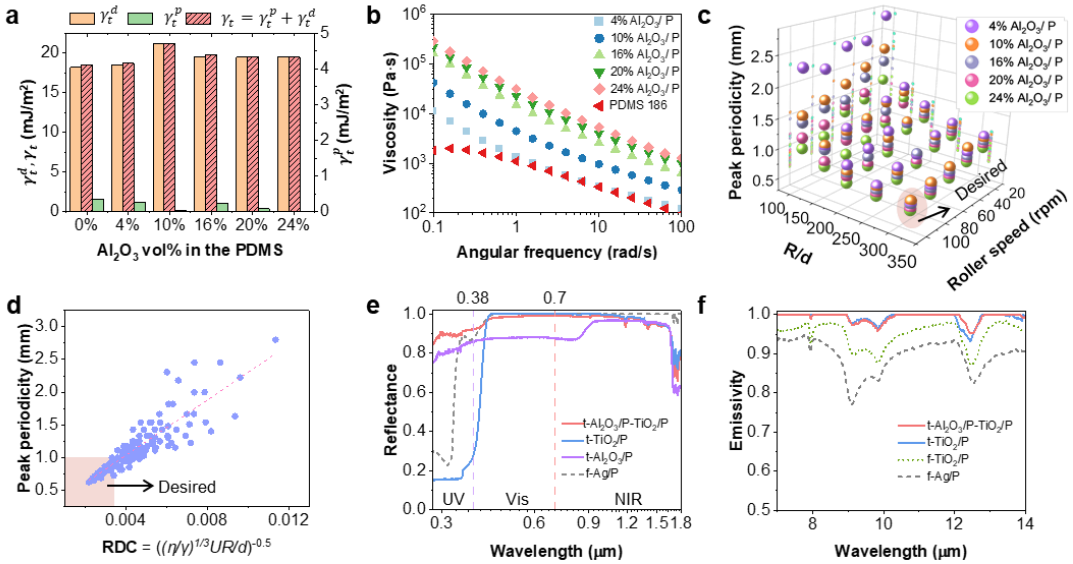

Fig. 4. (a) The surface energy components (polar, γ_t^d, disperse, γ_t^p, total, $\gamma_t = \gamma_t^p + \gamma_t^d$) of the different Al_2O_3 (200 nm) particle concentrations in PDMS (P). (b) Complex viscosity (η) vs. angular frequency. (c) A parametric experiment of the nanocomposite pastes, Peaks periodicity (p_{peak}) *vs.* Roller geometry factor (*R/d*) and roller speed (*U*). (d) Peak periodicity *vs.* Roll-to-roll defects coefficient (RDC). (e) The reflectance of a photonic coating sample (t- Al_2O_3/P-TiO_2/P) and other comparing samples on the solar spectrum. (f) The emissivity of the photonic coating and other comparing samples at mid-IR (7-14 μm). In the legend, t- is spike microstructured coating, f- is the flat coating, P is PDMS.

Outdoor measurements

To measure the daytime radiative cooling performance of the sample, a Peltier-based measurement platform was set up on a rooftop at Duke University, Durham, NC. The measurement system in Fig. 5(a-b) included a Peltier device, a PID controller, a data acquisition (DAQ) system, a power supply, and a thermopile pyranometer. The outdoor measurement was conducted in Durham on June 24th, 2022. Even if the temperature and solar radiation were as high as 32 ^oC and 806 W/m^2 in the summer noon (Fig. 5(c) and Fig. S16), the photonic coatings still achieved 99.2 W/m^2 averaged cooling power from 12:40 PM to 2:30 PM (excluding the cloudy periods), which matched the theoretical calculation results (102.9 W/m^2). It is worth noting that there were two partially cloudy periods during measurement (from 12:55 PM to 1:04 PM, and 2:17 PM to 2:30 PM) when pieces of small clouds only blocked the sun but not the entire view of the sky. During these periods, the measured cooling power was significantly elevated to around 130 W/m^2, because most of the solar heating was contributed by the direct solar radiation. Hence, significant solar heating was restricted by a small cloud. However, given the broad-angle high emissivity of the nanophotonic coatings (Fig. 2 (b) and 3(d)), the screening of the mid-IR radiation by the small clouds covering the sun was negligible. This cooling power elevating result also matched the experiment recorded in the reference, which suggested filtering out the directional solar radiation further improves daytime radiative cooling power [29]. The further test of the reference sample's (TiO_2/PDMS) cooling performance showed the benefit of having Al_2O_3 nanoparticles in the upper layer to scatter the UV radiation. The TiO_2/PDMS could only get cooling power as low as 39.0 W/m^2 due to the UV part absorption (Fig. 5(d)). The outdoor measurements demonstrated the efficacy of photonic design for boosting the daytime radiative cooling performance.

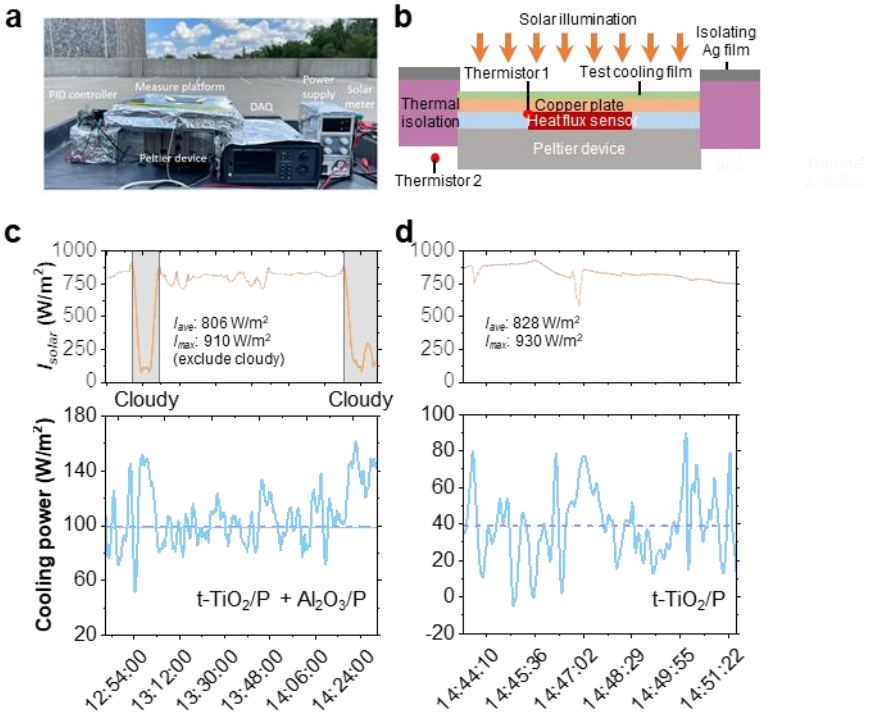

Fig. 5. (a) Peltier-based outdoor cooling power measurement platform set up on the rooftop at Duke University. (b) schematic of the Peltier-based measurement platform. (c) The cooling power measurement result of the bilayer photonic coatings and corresponding solar illumination, I_{solar} (average and maximum illumination were I_{ave} and I_{max}, respectively). (d) The cooling power measurement result of the single layer TiO_2/PDMS photonic coating and the corresponding, I_{solar}, I_{ave} and I_{max}. In the legend, t- was spike microstructured coating, f- was the flat coating, P was PDMS.

Building cooling energy saving

Inspired by the radiative cooling and self-cleaning capability, we proposed that the bilayer photonic coatings are able to serve as the efficient radiative coatings of the roofs for cooling energy saving in buildings (Fig. 6(a)). To quantitatively demonstrate the photonic coatings' scale-up impact on the building cooling efficiency, *EnergyPlus* with experimental measured materials' optical properties was imported to simulate the potential all-year cooling energy saving of the buildings across the US based on a scenario with mid-rise apartments. 15 cities corresponding to 15 climate zones in the US were chosen to calculate the cooling energy [7,28,30]. Compared with the baseline, buildings with radiative cooling roofs save energy up to 68.91 GJ/year in Phoenix, which constitutes 11.7% of the year-round cooling energy in the baseline buildings (Fig. 6(b)). As shown in the cooling energy saving map (Fig. 6(c)), the cooling materials benefit more in the hot and dry areas: 57.7 GJ/year in Honolulu (Climate zone number: 1A), 47.5 GJ/year in Austin (2A), 68.9 GJ/year in Phoenix (2B) and 42.6 GJ/year in LA (3B). Even if the temperature and solar radiation are high in these areas, the radiative cooling materials perform better because they reflect sunlight near perfectly and radiate more heat to the deep universe through the clear sky. However, the saving amount gradually decreases when the cooling materials are exposed to the weather in the cold areas: 9.7 GJ/year in Fairbanks (8) and 15.1 GJ/year in Duluth (7).This is because the cooling load is small in cold weather. Since the radiative photonic coating provides all-day cooling power when the space cooling is needed [28], by coating

the roof with our radiative cooling photonic coatings, about 33.4 GJ/year cooling energy may be saved on average over the entire US, which is also 15.1% of the year-round US cooling energy.

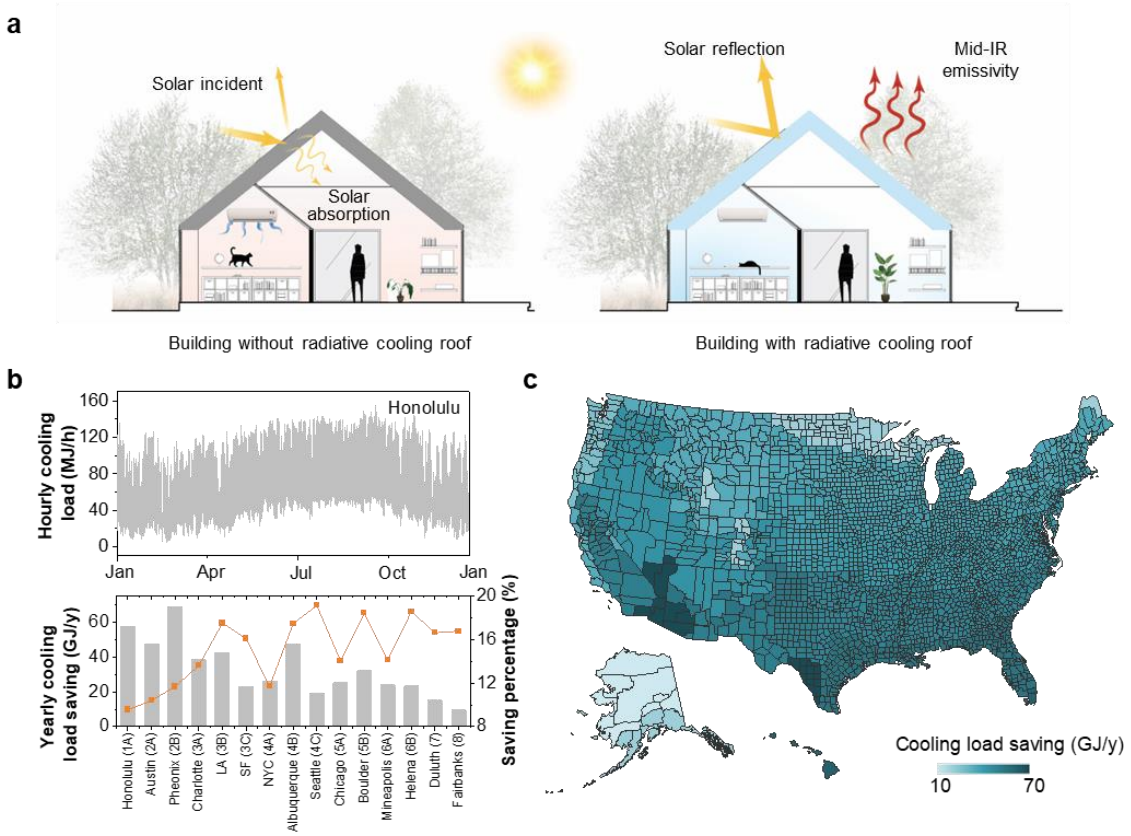

Fig. 6 (a) Schematic of the photonic coating applied on building cooling. (b) Building cooling energy saving simulation results in 15 cities corresponding to 15 climate zones in the U.S. compared with the baseline buildings (Honolulu as 1A climate zone example). (c) The cooling energy saving map of the U.S.

Discussion

In this research, we fabricated low-cost and scalable high-performance passive radiative cooling microstructured photonic coatings by a roll-to-roll method. By controlling the nanocomposite's viscosity and fabricating parameter (roller gap and speeds), periodical spike microstructures were generated spontaneously in the roll-to-roll process, which gave the materials 98.6% emissivity and strong superhydrophobic self-cleaning capability. A novel Roll-to-roll Defect Coefficient (RDC) was proposed to predict the peak periodicity by materials' viscoelastic properties and fabrication parameters. Such a photonic coating showed a 99.2 W/m^2 averaged cooling power under the direct sunlight. Benefiting from the high cooling power, scalable fabrication and superhydrophobic properties, the coating was proposed to serve as the cooling roofs. 15.1% of the year-round cooling energy saving around the US was demonstrated by numerical simulation.

More importantly, this fabrication method is compatible with any viscous composite paste and makes the scalable application of the photonic coatings possible. This research could potentially serve as a platform for broadening the applicability of the traditional roll-to-roll fabrication and inspire technological advancement in radiative cooling materials.

Methods

Roll coating procedure

The nanocomposite paste was prepared before the roll-to-roll process. The TiO_2 (500 nm) and Al_2O_3 (200 nm) were purchased from US-nano, Inc. The PDMS Sylgard 186 was purchased from Krayden, Inc. To prepare the nanocomposite paste, the TiO_2 and Al_2O_3 were mixed with PDMS Sylgard 186, respectively. The TiO_2 content was controlled to 25 vol% and Al_2O_3 is fabricated as 26 vol% which was pushed to the boundary of processability (too high particle content will lead to discontinuing paste). The hardener was introduced to the PDMS with a 10:1 weight ratio. The nanocomposites were preliminarily mixed by a universal planetary mixer for 10 mins. Then, the further mix was conducted in a high-shear three-roll milling machine. The roller distance was gradually decreased, and the pastes were processed five times for homogeneous nanoparticle dispersion.

The processed paste was collected and transferred to a two-roll coating machine. The diameter of each roller is 50.8 mm (2 inches). The two rollers were run independently, and the angular speed range is from 0 to 120 rpm. The prepared nanocomposite paste was put between two rollers, and the gap distance *d* and the roller speed *U* were manipulated carefully to obtain a micro-structured coating. Finally, the sample was cured at 120°C for 30 mins.

Surface characterization

The coating top surface 3D morphologies were characterized by the non-contacting laser scanning confocal microscope (Keyence VK-X1100, 0.5 nm height resolution, and 1 nm width resolution). The peak density data were evaluated from the laser confocal data. The surface morphology was also characterized by the scanning electron microscope (FEI Verios 460 L).

Liquid contact angle measurement

The water contact angle of the coatings was measured by the Ramé-hart goniometer (model 250, with the charge-coupled device camera and a 150 W fiber optic illuminator accessories) at ambient temperature (23°C). The consistent 2 μL liquid (water, glycerin, or Diindolylmethane) droplets were carefully dropped onto the sample surface. Then the syringe was retracted immediately. The images were captured at five different locations on each sample. Finally, the samples' water contact angles were measured by the low-bond axisymmetric drop shape analysis plugin provided by the ImageJ software. The surface energy calculation was based on Fowke's model and the Owens-Wendt model (SI.9) [20].

Rheology measurement

The dynamic oscillatory rheological properties of the nanocomposite were measured by Discovery Hybrid 3 rheometer (TA Instruments) with triplicate. A 25 mm cross-hatched parallel plate geometry was kept at 25 °C by using a Peltier plate. The trim gap of the rheometer head was controlled as 1100 μm at the beginning. Then, brought to 1000 μm after trimming. No pre-shearing was needed due to the sample ejecting in a shear deformation. The test was conducted immediately as viscometric parameters did not change after loading. The Elastic (G') and viscous (G") modulus can be directly achieved from the experiments. The complex viscosity (η) can be calculated by the equation:

$$\eta = \left[\left(\frac{G'}{\omega}\right)^2 + \left(\frac{G''}{\omega}\right)^2\right]^{0.5} \quad (1)$$

Where ω is the angular frequency.

Optical finite element analysis of the microstructure

The emissivity of the microstructure coating was simulated in finite element analysis software (COMSOL Multiphysics, 5.5. Wave optics physics). The volume of PDMS (nanocomposite) was controlled as constant to prevent the thickness effect. The top side of the model was set as Port 1 with incident light and the bottom was set as Port 2. Other boundaries were set as periodic boundary conditions. The reflectivity (R) and the absorptivity (A) can be obtained from the COMSOL simulation. The material emissivity can be calculated by equation according to the Kirchhoff's law:

$$E = A/(1 - R) \tag{2}$$

Spectrometry characterization.

The reflectance was measured by UV–visible–NIR spectroscopy spectrometer (UV-Vis, 300–2000 nm, Agilent technologies, Cary 6000i) with a calibrated $BaSO_4$ integrating sphere and $BaSO_4$ reference at 0.3-1.8 μm. The coatings' emittance was characterized by a Fourier Transform Infrared spectrometer (FTIR, 4–18 μm, Thermo Scientific, iS50) with a diffuse gold integrating sphere.

Measurement of radiative cooling power

The basic principle of the measurement is to suppress the convective loss to/from the ambient by minimizing the temperature difference between the ambient and the sample. Hence, the cooling power measurement was conducted above the Peltier device under ambient temperature. Specifically, in Fig. 5(b), the two thermistors are used to record the ambient and sample temperature, respectively. Then the signal will be transferred to the PID controller through the DAQ and laptop. The PID program controls the Peltier device to supply heating/cooling power to the sample to compromise the radiative cooling/solar heating power. At thermal equilibrium, the heat flux sensor beneath the Cu plate measures the heat flux supplied by the Peltier device. Such a heat flux is equal to the solar heating (downward) or radiative cooling (upward) flux. All the experiment platform's thermistors and heat flux sensors are connected to the DAQ and recorded by the laptop. The daytime radiative cooling power was recorded when the sample temperature was equal to the ambient temperature. This minimizes the convective loss and thus improves the accuracy of the measurement. In the experimental set-up shown in Fig. 5(b), the sample was attached to the Cu plate (Width: 5 cm, Length: 5 cm, Thickness: 1.5 mm) by thermal grease (Dow Corning, 340). The 1mm thick heat flux sensor (Electro Optical Components, Inc., A-04457) is surrounded by glass slides. The temperature was measured by the thermistor (TE Technology Inc., TC-36-25). The PID-controlled Peltier device (TE Technology Inc., TC-36-25) was used to supply the heating/cooling power adaptive to solar heating/radiative cooling. Before measurement, the calibration of the testing apparatus was performed based on our previous method[28].

Building Energy Simulation

EnergyPlus version 9.4 was employed to predict the cooling energy consumption and saving with different roof coatings across the US. We chose fifteen cities to represent the 15 climate zones in the US. For the building model, the New-2004 Mid-rise apartment model with four stories and 3135 m^2 area, given by the US Department of Energy, was utilized for simulation. The TMY2 hourly weather data was used as the external environment

boundary conditions of the simulation. The cooling load power (P_{cool}) was calculated by running the software hourly through the whole year. Then, the hourly cooling energy consumption was obtained by $E_{cool,\ hour} = 3600 \times P_{cool}$. Finally, the whole year cooling energy consumption was estimated by summing up the whole year $E_{cool,\ hour}$.

Acknowledgment

This research is based upon work supported by the start-up fund by Pratt School of Engineering, Duke University (P. Hsu), NCSU Faculty Research and Professional Development award (J. Ryu), and National Science Foundation under grant No. 2031558. Part of this work was performed at the Analytical Instrumentation Facility (AIF) at North Carolina State University, which is supported by the State of North Carolina and the National Science Foundation (award number ECCS-2025064). We also thanks Dr. Benjamin J. Wiley for the help of the UV-Vis measurement.

Author contributions

P. Hsu and J. Ryu conceived and planned the study; S. Liu, C. Sui, M. Harbinson, M. Pudlo, H. Perera and Y. Liu performed the experiments; S. Liu, Z. Zhang, R. Liu, Z. Ku performed the simulation. S. Liu, C. Sui, H. Perera, Y. Zhu, J. Genzer, S. Khan, P. Hsu and J. Ryu performed data analysis. S. Liu, C. Sui, P. Hsu and J. Ryu wrote the paper. All authors discussed the results and approved the final version of the paper.

Reference:

1. US Department of Energy. 2010 Residential Energy End-Use Expenditure Splits, by Fuel Type. *Build. Energy Data Book* (2012). URL: http://192.31.135.76/TableView.aspx?table=2.3.5
2. Chu, S. & Majumdar, A. Opportunities and challenges for a sustainable energy future. *Nature* **488**, 294–303 (2012).
3. Zhang, H. *et al.* Biologically inspired flexible photonic films for efficient passive radiative cooling. *Proc. Natl. Acad. Sci. U. S. A.* **117**, 14657–14666 (2020).
4. Mandal, J. *et al.* Hierarchically porous polymer coatings for highly efficient passive daytime radiative cooling. *Science* **362**, 315–319 (2018).
5. Li, X., Peoples, J., Yao, P. & Ruan, X. Ultrawhite BaSO4Paints and Films for Remarkable Daytime Subambient Radiative Cooling. *ACS Appl. Mater. Interfaces* **13**, 21733–21739 (2021).
6. Zhai, Y. *et al.* Scalable-manufactured randomized glass-polymer hybrid metamaterial for daytime radiative cooling. *Science* **355**, 1062–1066 (2017).
7. Li, T. *et al.* A radiative cooling structural material. *Science* **364**, 760–763 (2019).
8. Li, D. *et al.* Scalable and hierarchically designed polymer film as a selective thermal emitter for high-performance all-day radiative cooling. *Nat. Nanotechnol.* **16**, 153–158 (2021).
9. Jeong, S. Y., Tso, C. Y., Wong, Y. M., Chao, C. Y. H. & Huang, B. Daytime passive radiative cooling by ultra emissive bio-inspired polymeric surface. *Sol. Energy Mater. Sol. Cells* **206**, 110296 (2020).
10. Raman, A. P., Anoma, M. A., Zhu, L., Rephaeli, E. & Fan, S. Passive radiative cooling below ambient air temperature under direct sunlight. *Nature* **515**, 540–544 (2014).
11. Hsu, P.-C. *et al.* Radiative human body cooling by nanoporous polyethylene textile. *Science* **353**, 1019–1023 (2016).

12. Leroy, A. *et al.* High-performance subambient radiative cooling enabled by optically selective and thermally insulating polyethylene aerogel. *Sci. Adv.* **5**, eaat9480 (2019).
13. Shi, N. N. *et al.* Keeping cool: Enhanced optical reflection and radiative heat dissipation in Saharan silver ants. *Science* **349**, 298–301 (2015).
14. Castillo, M. E. G. & Patera, A. T. Three-dimensional ribbing instability in symmetric forward-roll film-coating processes. *J. Fluid Mech.* **335**, 323–359 (1997).
15. Chong, Y. H., Gaskell, P. H. & Kapur, N. Coating with deformable rolls: An experimental investigation of the ribbing instability. *Chem. Eng. Sci.* **62**, 4138–4145 (2007).
16. Bauman, T., Sullivan, T. & Middleman, S. Ribbing instability in coating flows: effect of polymer additives. *Chem. Eng. Commun.* **14**, 35–46 (1982).
17. Greener, J., Sullivan, T., Turner, B. & Middleman, S. Ribbing instability of a two-roll coater: Newtonian fluids. *Chem. Eng. Commun.* **5**, 73–83 (1980).
18. Abbasi, S., Zebarjad, S. M., Baghban, S. H. N., Youssefi, A. & Ekrami-Kakhki, M.-S. Experimental investigation of the rheological behavior and viscosity of decorated multi-walled carbon nanotubes with TiO2 nanoparticles/water nanofluids. *J. Therm. Anal. Calorim.* **123**, 81–89 (2016).
19. Jo, B. & Banerjee, D. Viscosity measurements of multi-walled carbon nanotubes-based high temperature nanofluids. *Mater. Lett.* **122**, 212–215 (2014).
20. Islam, M. D. *et al.* Template-Free Scalable Fabrication of Linearly Periodic Microstructures by Controlling Ribbing Defects Phenomenon in Forward Roll Coating for Multifunctional Applications. *Adv. Mater. Interfaces* 2201237 (2022).
21. Fields, R. J. & Ashby, M. F. Finger-like crack growth in solids and liquids. *Philos. Mag.* **33**, 33–48 (1976).
22. Lee, J. H., Han, S. K., Lee, J. S., Jung, H. W. & Hyun, J. C. Ribbing instability in rigid and deformable forward roll coating flows. *Korea-Australia Rheol. J.* **22**, 75–80 (2010).
23. Grillet, A. M., Lee, A. G. & Shaqfeh, E. S. G. Observations of ribbing instabilities in elastic fluid flows with gravity stabilization. *J. Fluid Mech.* **399**, 49–83 (1999).
24. Bohren, C. F. & Huffman, D. R. *Absorption and scattering of light by small particles*. (John Wiley & Sons, 2008).
25. Li, D. *et al.* Scalable and hierarchically designed polymer film as a selective thermal emitter for high-performance all-day radiative cooling. *Nat. Nanotechnol.* **16**, 153–158 (2021).
26. Mandal, J. *et al.* Hierarchically porous polymer coatings for highly efficient passive daytime radiative cooling. *Science* **362**, 315–319 (2018).
27. Yu, X., Chan, J. & Chen, C. Review of radiative cooling materials: Performance evaluation and design approaches. *Nano Energy* **88**, 106259 (2021).
28. Li, X. *et al.* Integration of daytime radiative cooling and solar heating for year-round energy saving in buildings. *Nat. Commun.* **11**, 1–9 (2020).
29. Bhatia, B. *et al.* Passive directional sub-ambient daytime radiative cooling. *Nat. Commun.* **9**, 1–8 (2018).
30. Baechler, M. C. *et al. Building America best practices series: volume 7.1: guide to determining climate regions by county*. (2010).

Supplementary information

Sample surface characterization

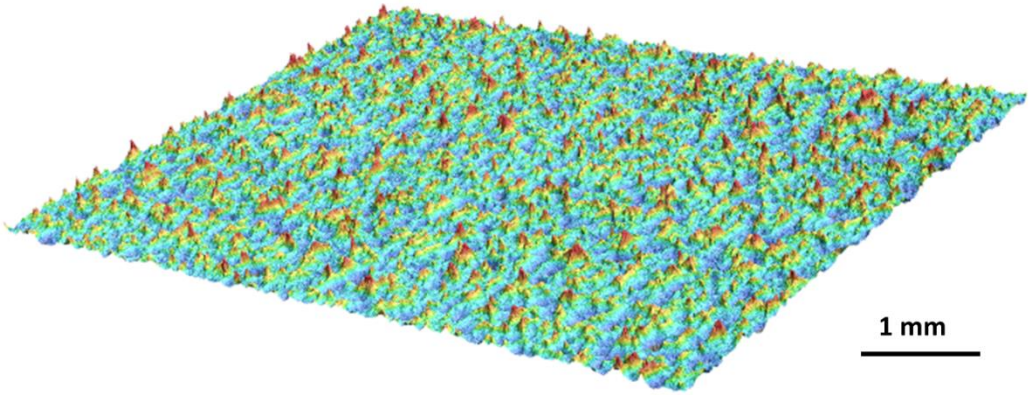

The laser confocal picture of the Al_2O_3/polydimethylsiloxane (PDMS) - TiO_2/PDMS surface.

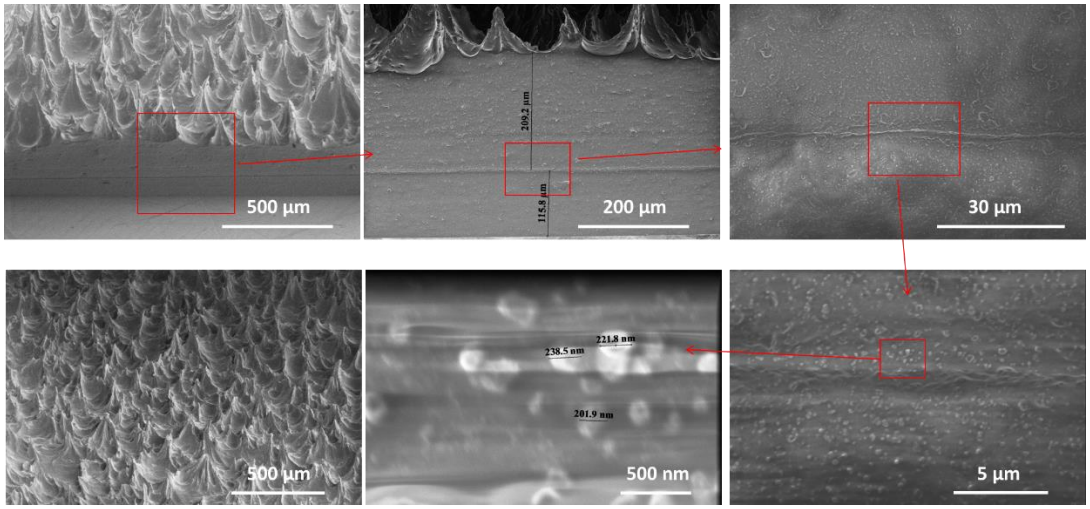

The SEM pictures of the Al_2O_3/polydimethylsiloxane (PDMS)-TiO_2/PDMS surface.

Theoretical passive radiative cooling power calculations

The blackbody radiation of an object with absolute temperature *T* at wavelength (λ) can be calculated by Planck's laws:

$$I_{BB}(T,\lambda) = \frac{2hc^2}{\lambda^5}\frac{1}{e^{\frac{hc}{\lambda kT}}-1} \quad \text{(S1)}$$

where h is the Plank constant, *c* is the speed of light, and *k* is the Boltzmann constant. The radiative power density of film can be calculated by integrating the spectral radiance density over atmosphere long-wave infrared radiation (LWIR) transmission windows, 7-14 μm:

$$p_{rad}(T) = 2\pi \int_0^{\frac{\pi}{2}} \int_{7\,\mu m}^{14\,\mu m} I_{BB}(T,\lambda)\epsilon_{film}(\lambda,\theta)\, sin\theta\, cos\theta\, d\lambda d\theta \quad \text{(S2)}$$

Where $\epsilon_{film}(\lambda,\theta)$ is the spectral emissivity (absorptivity) of the film. The aborted radiative power density by atmosphere can be obtained by:

$$p_{amb}(T_{amb}) = 2\pi \int_0^{\frac{\pi}{2}} \int_{7\,\mu m}^{14\,\mu m} I_{BB}(T,\lambda)\epsilon_{film}(\lambda,\theta)\epsilon_{atm}(\lambda,\theta)\, sin\theta cos\theta\, d\lambda d\theta \quad \text{(S3)}$$

Where T_{amb} is the ambient temperature (it was assumed same as the film temperature *T*) and $\epsilon_{atm}(\lambda,\theta)$ is the atmospheric emissivity (absorptivity). Considering the humidity and the cloud cover effect, the atmospheric emissivity ϵ_{atm} was corrected by an equation:

$$\epsilon_{atm} = \epsilon_{atm,c}(1 - 0.78CF) + 0.38CF0.95\, RH0.17 \quad \text{(S4)}$$

Where $\epsilon_{atm,c}$ is the sky emissivity under clear skies, *CF* is the cloud fraction, *RH* is the ambient relative humidity. The $\epsilon_{atm,c}$ was calculated by a web-based software provided by SOFIA Science Center – ATRAN.

$$p_{cool} = p_{rad} - p_{amb} - h_L\Delta T - I\beta \quad \text{(S5)}$$

where h_L is the heat transfer coefficient of convective and conductive loss, ΔT is the temperature difference between cooling material surface and environment (it was assumed as 0). *I* is the solar radiation power density at Durham, NC, USA. β is the sunlight absorption coefficient of film.

Literature comparing:

Seven remarkable references were chosen to compare with our product [1–7]. The theoretically solar radiation absorption ($I\beta$), LWIR radiative power (p_{rad}), and cooling power (p_{cool}) were calculated by equation S1 – S5 according to optical characteristics (solar reflectance (*R*) and LWIR emissivity (*E*)) recorded in the reference. The weather conditions were normalized at 32 ºC, 50% humidity and 20% cloudy cover rate, 800 W/m^2 solar radiation power and 400 ft elevation and 36° N latitude (Durham's coordination). The maximum radiative power is 124.7 W/m in this environment assumption. The detailed comparison was shown in Table S1 and Fig. 2(c).

Table S1. Literature comparing summary

Reference	Design	Manufacturing	Feature	R	E	$I\beta$ W/m^2	p_{rad} W/m^2	p_{cool} W/m^2
Zhang, 2020 [1]	· Metasurface Al_2O_3-PDMS	· Metasurface, lithography	· Enhanced *E* by bio-inspired metasurface	93.8%	95.7%	49.6	119.3	69.7
Mandal, 2018 [2]	· Porous P(VdF-HFP)$_{HP}$	· Porous polymer, · Need solvent	· High *R* by porous backscattering	96.5%	97.0%	28	120.9	92.9
Li, 2021 [3]	· $BaSO_4$-Acrylic film	· Dissolve and dispersion.	· High *R*	97.7%	95.3%	18.4	118.8	100.4
Zhai, 2017 [4]	· SiO_2/PMP/Silver film	· Roll to roll	· Scalable · Silver coating	94.7%	92.6%	42.4	115.4	73.0
Li, 2019 [5]	· Modified wood	· Modify wood	· High strength	91.7%	90.3%	66.4	112.6	46.2
Li, 2021 [6]	· PEO fiber textile	· Polymer fiber electrospinning	· Textile. · Scalable	96.1%	74.6%	31.2	93.0	61.8
Jeong, 2020 [7]	· Metasurface PDMS-SiO_2-Silver	· Metasurface bio-inspired, need lithography	· Enhanced *E* by bio-inspired metasurface.	96.7%	93.7%	26.4	116.8	90.4
Our work	· Metasurface Al_2O_3-TiO_2-PDMS	· Roll-to-roll, template-free.	· Template free metasurface. High *R*.	97.6%	98.5%	20	122.9	102.9

Note:

Poly (vinylidene fluoride-co hexafluoropropene) [P(VdF-HFP)$_{HP}$]

Polydimethylsiloxane [PDMS]

Polymethylpentene [PMP]

Polyethylene oxide [PEO]

Film contamination test

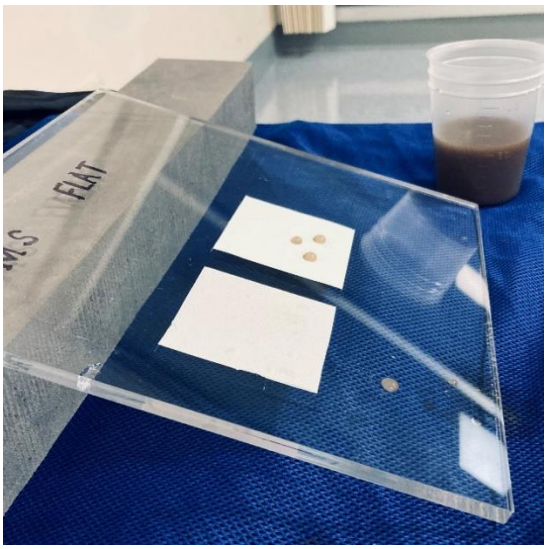

The surface contamination resistance test where tilt angle is 30^{o}.

Backscattering calculation based on Mie theory:

According to the Mie theory, there are:

$$Q_i = \frac{\sigma_i}{\pi a^2} \quad \text{(S6)}$$

The efficiencies Q_i is for the interaction of radiation with a scattering sphere (nanoparticles in our case). a is the radius of the scattering sphere. σ_i is the normalized to the particle cross section area, πa^2, where *i* stands for extinction (*i*=*ext*), absorption (*i*=*abs*), scattering (*i*=*sca*), forward scattering (*i*=*f*), backscattering (*i*=*b*).

There is relation between extinction, scattering and absorption induced by scattering sphere:

$$\sigma_{ext} = \sigma_{sca} + \sigma_{abs} \quad \text{(S7)}$$

$$\text{or } Q_{ext} = Q_{sca} + Q_{abs} \quad \text{(S8)}$$

$$x = ka \quad \text{(S9)}$$

$$k = 2\pi/\lambda_m \quad \text{(S10)}$$

$$Q_{sca} = \frac{2}{x^2}\sum_{n=1}^{\infty}(2n+1)(|a_n|^2 + |b_n|^2) \quad \text{(S11)}$$

$$Q_b = \frac{1}{x^2}\left|\sum_{n=1}^{\infty}(2n+1)(-1)^n(a_n - b_n)\right|^2 \quad \text{(S12)}$$

$$n_{max} \approx x + 4x^{1/3} + 2 \quad \text{(S13)}$$

Where the *x* is the size parameter, *k* is the wavenumber, λ_m is the incident radiation wavelength in medium (polymer matrix, PDMS, in this study) and a_n and b_n are Mie coefficients to compute the amplitudes of the scattered field. The detailed calculation of a_n and b_n are recorded in the reference [8].

Note that the efficiency Q_i is calculated for individual scattering sphere. To considering sphere concentration's effect, the coefficient α_i can be calculated:

$$\alpha_i = N\sigma_i \quad \text{(S14)}$$

$$\alpha_b = N\sigma_b \quad \text{(S15)}$$

where N is the scattering sphere concentration in the matrix material.

The backscattering coefficient was calculated for Al_2O_3 (50 nm - 1000 nm) and TiO_2 (50 nm - 1000 nm), respectively. The particles concentrations were set as 25 vol% (near to the process limitation of the Al_2O_3) or TiO_2 nanocomposite paste in PMDS. The matrix material was set as PDMS. The Mie calculations were conducted for the incident wavelength range from 0.3-2.0 um.

Nanoparticle backscattering calculations

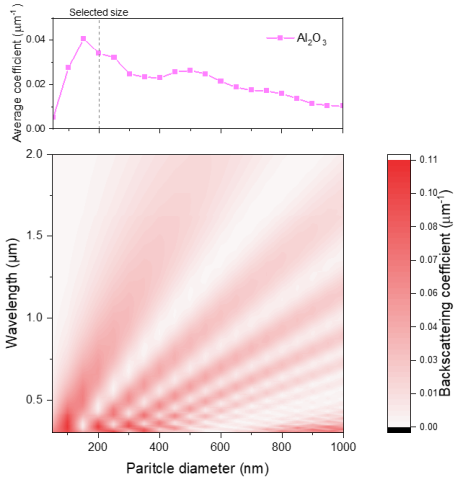

Al_2O_3 nanoparticles backscattering coefficient calculation at wavelength 0.3-2.0 μm.

Optical simulation of microstructure's effect on solar reflectivity

The microstructures' effect on the solar reflectivity was simulated by the Rigorous Coupled-Wave Analysis (RCWA). The RCWA model was shown in the 0. The air and PDMS substrate thickness were infinite. The left and right sides of the model were set as periodic boundary conditions. The RCWA model's triangular topography was sliced into *n* layers. The designed topography with height (*h*) = 30 μm, pitch length (*p*) = 100 μm and base length (*b*) = 30 μm was used for the simulation. For all the simulations in this chapter, the incident wavelength was set as 0.3 - 2 μm, the incident angle was 0 – 70 ºC, diffraction order was ±5, and the incident polarization was TM+TE.

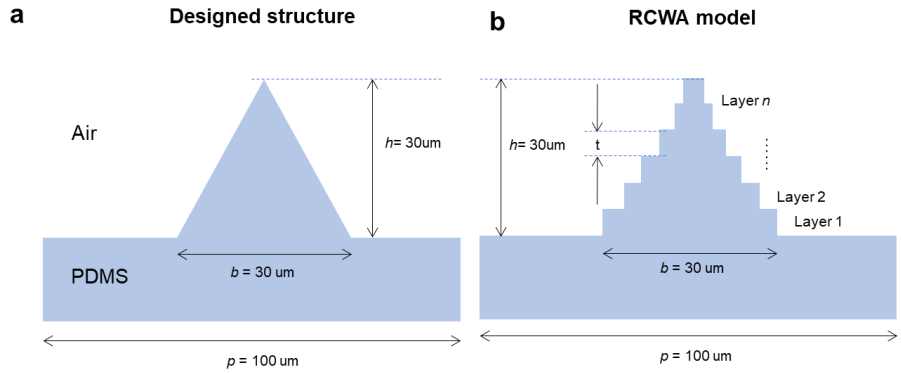

(a) designed structure topography diagram, (b) The sliced topography RCWA model diagram.

Slice layers effect

When the layers number *n* was large enough, the layer stacked topography (0(b)) could be considered as a continue topography (0(a)). The slice layers effect was investigated. The designed topography was sliced into 50, 100, and 200 layers. The simulation results were shown in the 0. When the layer number is larger than 50, there is only negligible effect led by the layers number.

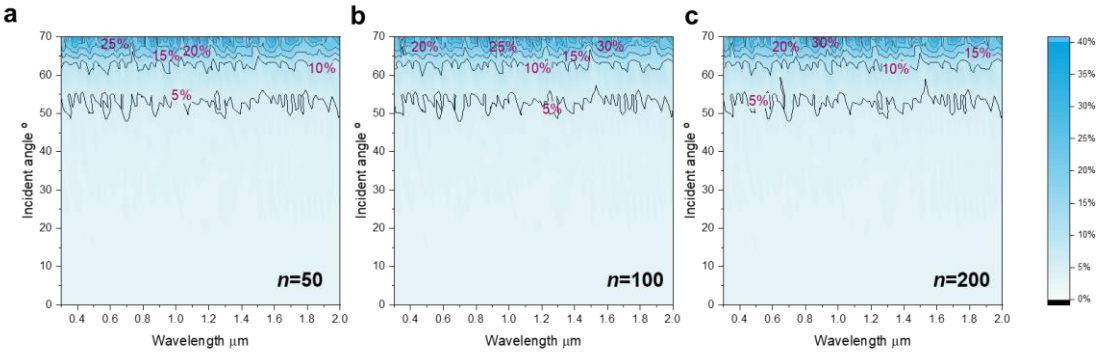

The slice layers number (*n*) effect of the RCWA model, (a) *n*=50, (b) *n*=100, (c) *n*=200.

Triangular topography's effect to solar reflectivity

The slice layers number was set as 200. The solar reflectivity simulation results of the triangular topography model and the flat mode were shown in the 0 and Fig. 2(c). The topography with the size (p=100 um, b= 30um, h=30 um) did not have significant influence on the solar reflectance at range 0.3 - 2 um. Especially when the incident angle is smaller than 50º, the reflectance difference with flat PDMS surface is near to 0. The triangular topography showed an average reflectance as 6.6%, where the flat film showed as 7.9%.

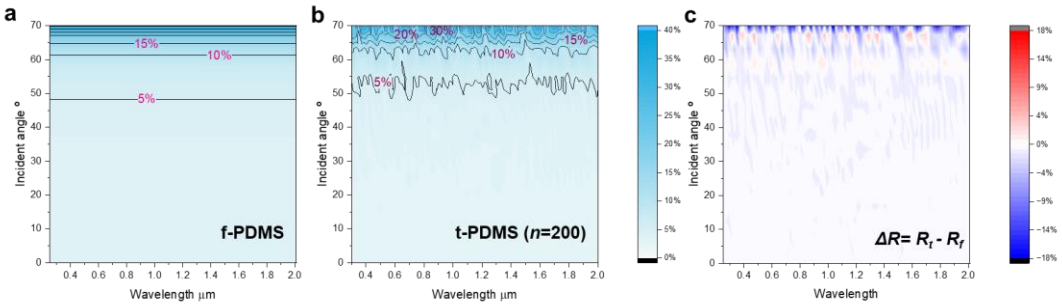

Triangular topography's effect to solar reflectivity simulation results by RCWA, (a) f-PDMS reflectivity (R_f), (b) t-PDMS reflectivity (R_t), n=200, (c) The reflectance different ($\Delta R = R_t - R_f$) between f-PDMS and t-PDMS.

Optical finite element analysis of the microstructure's LWIR emissivity.

The emissivity of the microstructures film was simulated in finite elements analysis software (COMSOL Multiphysics, 5.5. Wave optics physics.). To investigate the effects of the spike microstructure, 2D models were built (0). The topside of the model was set as port 1 (0, orange line) with incident light and the bottom as set as port 2 (0, purple line). Other boundaries were set as periodic (0, green line). The reflectance (*R*) and the absorptance (*A*) can be obtained from the COMSOL simulation for both TM and TE incident waves. The *R* or *A* average value of TM and TE was used for the calculation. The material emittance can be calculated by equation:

$$E = \frac{A}{1-R} \tag{S16}$$

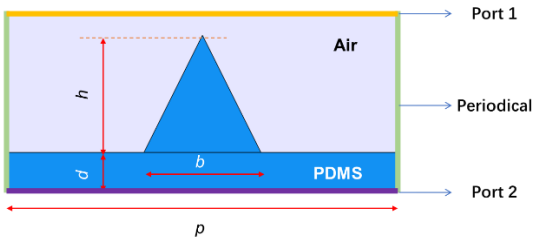

The FEA model and the boundary conditions of the triangular structured topography in COMSOL.

Topography shape effect on LWIR emissivity

The different microstructures' shape effects to the LWIR emissivity were simulated. The reference flat PDMS model was controlled with the same PDMS volume with another microstructure model, and the triangular, square, and circular topography were controlled in the same volume, side length / diameter are 30, 21.21, 23.94 μm, respectively. The results showed that all the triangular, square, and circular topography can significantly enhance the LWIR emissivity (0). The circular and square topography have comparable emissivity (~85%), and the triangular topography's emissivity (87.0 %) was slightly higher than others (0). The model's electrical field maps were shown in the 0. The volume PDMS (nanocomposite) were controlled as constant to prevent the thickness effect of absorption.

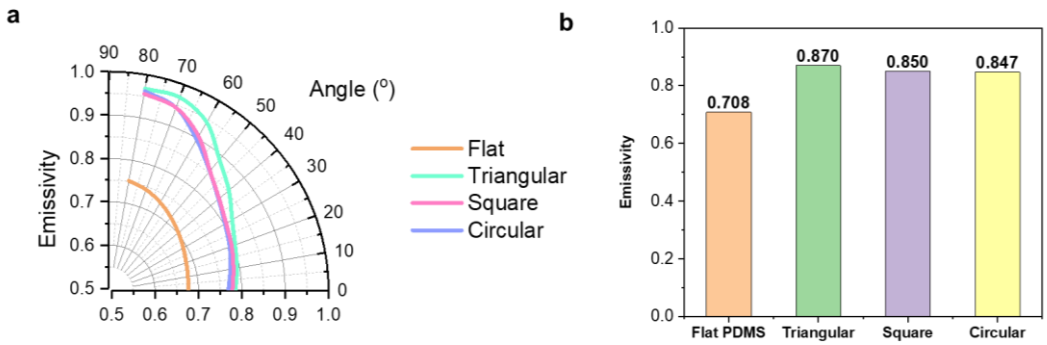

The simulation results of topography shape effect on LWIR emissivity

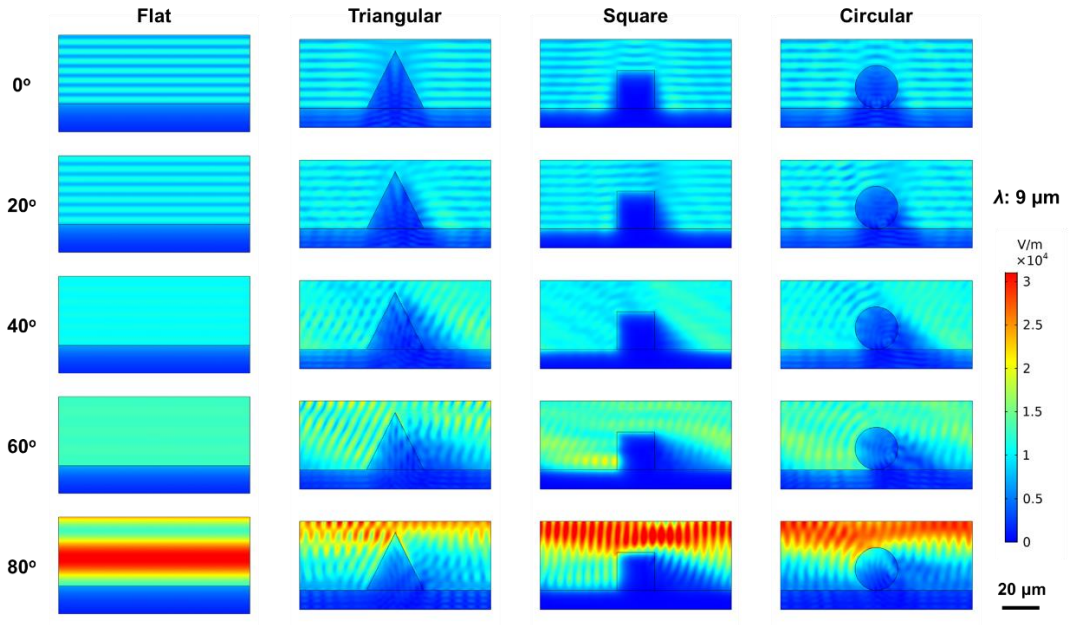

The simulation electric filed maps of topography shape effect on LWIR emissivity

Topography and nanoparticle combined effect

To investigate the combined effect of nanoparticles and topography (that are the situation in our roll-to-roll film), the flat and topography model with 25 vol% Al_2O_3/PDMS and 25 vol% TiO_2/PDMS were simulated, respectively. The model's size parameters are p =100 μm, b = 30 μm, d = 10 μm, and the h=30 μm. The simulations were conducted the incident angle as 0-80° with step length as 10°. The effective refractive index of the nanocomposites (25 vol% Al_2O_3/PDMS and 25 vol% TiO_2/PDMS) were estimated by Lorentz-Lorenz formula.

$$\frac{n^2-1}{n^2+2} = (1-f_v)\frac{n_2^2-1}{n_2^2+2} + f_v\left(\frac{n_1^2-1}{n_1^2+2}\right) \quad \text{(S17)}$$

Where f_v is the volume fraction of nanoparticles, n_1 and n_2 are the refractive index of nanoparticles and matrix consecutively, and n is the effective refractive index of the composite. The effective refractive index of the nanocomposites were used in the simulation.

The simulation results are shown in the Fig. 3(d) and 0.

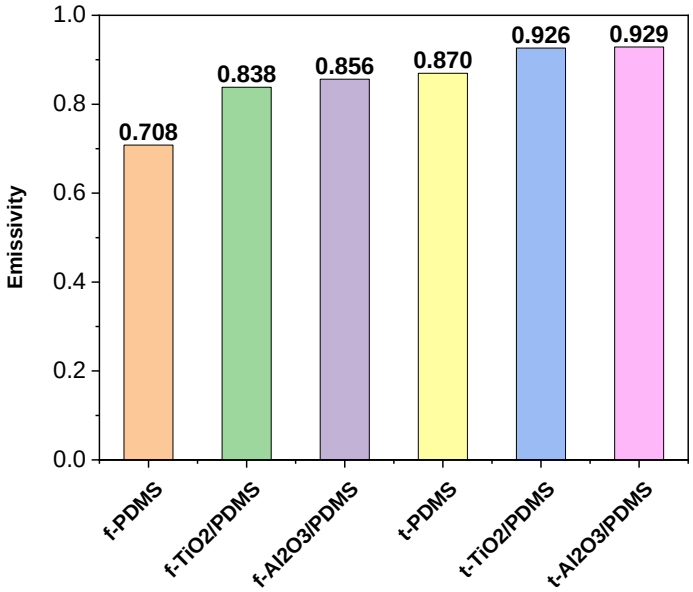

The simulation results of topography and nanoparticle combined effect on LWIR emissivity.

Topography scale effect

The topography height (*h*) and pitch length (*p*) effects were simulated, respectively. For the height effect simulation, *p* =100 μm, base length (*b*) = 30 μm, *d* = 10 μm, and the *h* changed from 10 μm to 50 μm with step length as 4 μm. For the pitch length effect simulation, *h* =30 μm, *b* = 30 μm, *d* = 10 μm, and the *p* changed from 20 μm – 200 μm with step length as 10 μm. The incident angle was 0°. The results show that higher topography and smaller pitch length will lead to a high emissivity (0).

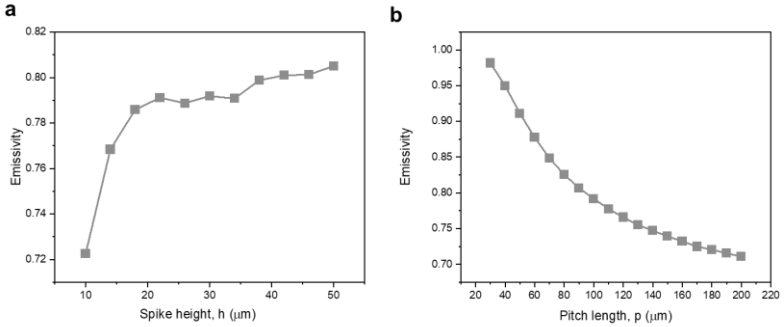

The topography scale effects, (a) heigh (*h*) effect, (b) pitch length (*p*) effect.

Roll-to-Roll manufacturing

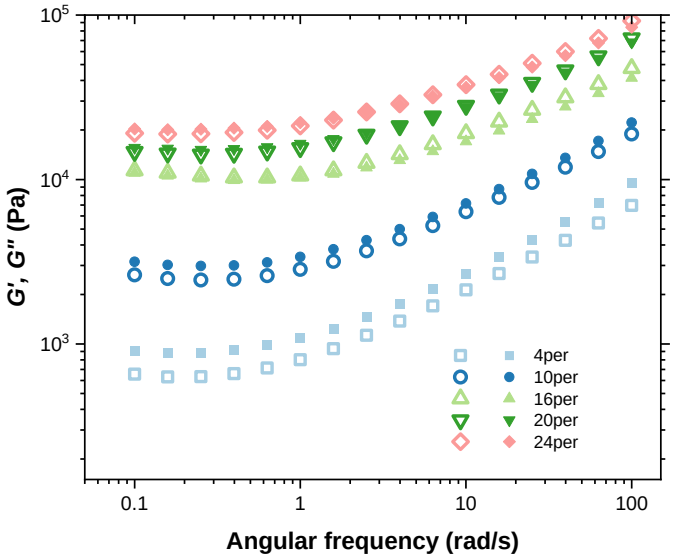

Elastic (G') and viscous (G") modulus of Al_2O_3/PDMS nanocomposite as a function of angular frequency.

Apparent surface energy

In this study, Fowke's model[9] and the Owens-Wendt model[10,11] were employed to derive the surface energy from the liquid contact angle data. Fowke's model and Young-Dupre equation separated the liquid and solid materials' surface energy as polar and non-polar (disperse) components. For here, γ_l^d and γ_l^p are liquid non-polar(dispersive) and polar components, respectively; γ_s^d and γ_s^p are the solid non-polar and polar components. Three reference liquids (e.g., water, diiodomethane (99%), and glycerin (99%)) with known surface energy value (Table S2) were used to estimate the surface energy of the tested solid film. There was a surface energy relation between the liquid and the tested solid:

$$\frac{\gamma_l(cos\theta+1)}{2} = \left(\gamma_l^d\right)^{1/2}\left(\gamma_s^d\right)^{1/2} + \left(\gamma_l^p\right)^{1/2}\left(\gamma_s^p\right)^{1/2} \quad \text{(S18)}$$

$$\frac{\gamma_l(cos\theta+1)}{2\left(\gamma_l^d\right)^{1/2}} = \left(\gamma_s^d\right)^{1/2} + \frac{\left(\gamma_l^p\right)^{1/2}\left(\gamma_s^p\right)^{1/2}}{\left(\gamma_l^d\right)^{1/2}} \quad \text{(S19)}$$

Where θ is the liquid contact angle on the solid surface. Finally, the γ_s^d and the γ_s^p can be obtained by fitting the known liquid surface energy and measured contact angle data. The intercept of the linear fitting equation is the γ_s^d, and the slope is γ_s^p.

Table S2. Polar and dispersive surface energy components of the test liquids[12]

Test liquid	γ_l (mJ m^{-2})	γ_l^p (mJ m^{-2})	γ_l^d (mJ m^{-2})
Water	72.8	51.0	21.8
Diiodomethane (DIM)	50.8	0.0	50.8
Glycerin	64.0	30.0	34.0

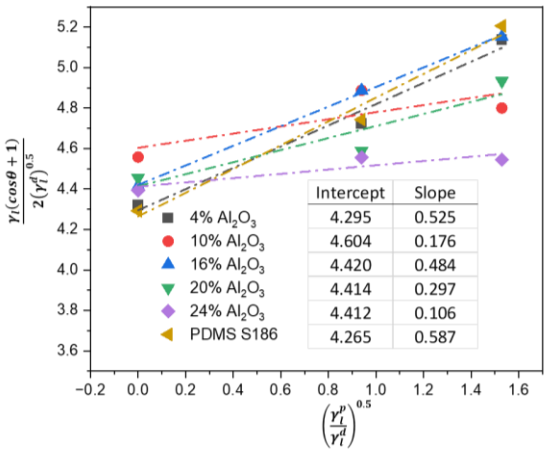

The test materials are analyzed for contact angle for various reference liquids, and the results in data are fitted in the Owens-Wendt model.

Table S3. Liquid contact angle measurement of Al_2O_3/PDMS nanocomposite. γ_l^d and γ_l^p are liquid non-polar(dispersive) and polar components, respectively; γ_s^d and γ_s^p are the Al_2O_3/PDMS nanocomposite non-polar and polar components, respectively.

Material	**Test liquid**	**Liquid contact angle, θ**	$\frac{\gamma_l^p}{\gamma_l^d}$	$\frac{\gamma_l(cos\theta+1)}{2(\gamma_l^d)^{1/2}}$	γ_s^d **(mJ m^{-2})**	γ_s^p **(mJ m^{-2})**	$\gamma_s = \gamma_s^p + \gamma_s^d$ **(mJ m^{-2})**
PDMS Sygarld 186	Water	109.4	1.53	5.21	0.34	18.19	18.53
	Glycerin	97.8	0.94	4.74			
	DIM	78.2	0.00	4.29			
4 vol% Al_2O_3/PDMS	Water	109.9	1.53	5.14	0.28	18.44	18.72
	Glycerin	98.0	0.94	4.72			
	DIM	77.8	0.00	4.32			
10 vol% Al_2O_3/PDMS	Water	112.6	1.53	4.80	0.03	19.48	19.57
	Glycerin	96.3	0.94	4.89			

	DIM	73.8	0.00	4.56			
16 vol% Al_2O_3/PDMS	Water	109.8	1.53	5.15	0.23	21.19	21.23
	Glycerin	96.3	0.94	4.89			
	DIM	76.2	0.00	4.41			
20 vol% Al_2O_3/PDMS	Water	111.5	1.53	4.93	0.09	19.46	19.47
	Glycerin	99.4	0.94	4.59			
	DIM	75.5	0.00	4.45			
24 vol% Al_2O_3/PDMS	Water	114.6	1.53	4.55	0.01	19.54	19.77
	Glycerin	99.8	0.94	4.56			
	DIM	76.5	0.00	4.39			

Parametric manufacturing data.

Table S4. Roll-to-roll parametrical fabrication experiments data summary of Al_2O_3/PDMS nanocomposite, where the roller radius *R* is 50 mm.

Material	***d* (mm)**	***R/d***	**Peak distance (mm)**				
			***U*=20 rpm**	***U*=40 rpm**	***U*=60 rpm**	***U*=80 rpm**	***U*=100 rpm**
4% Al_2O_3/PDMS	0.25	102	2.801	2.451	2.451	2.179	2.307
	0.17	150	1.634	1.508	1.307	1.307	1.153
	0.13	196	1.401	1.225	1.225	1.089	0.980
	0.1	255	1.225	1.153	0.980	0.934	0.817
	0.08	319	1.153	1.032	0.853	0.817	0.726
10% Al_2O_3/PDMS	0.25	102	2.222	2.000	1.818	1.667	1.538
	0.17	150	1.538	1.481	1.333	1.250	1.176
	0.13	196	1.333	1.250	1.111	0.952	0.870
	0.1	255	1.176	1.143	1.000	0.870	0.800
	0.08	319	1.111	1.111	0.952	0.870	0.769
16% Al_2O_3/PDMS	0.25	102	2.000	1.818	1.538	1.538	1.429
	0.17	150	1.429	1.333	1.250	1.176	1.111
	0.13	196	1.250	1.212	1.000	0.952	0.833
	0.1	255	1.111	1.053	1.000	0.800	0.741
	0.08	319	1.053	0.952	0.870	0.769	0.714
20% Al_2O_3/PDMS	0.25	102	1.667	1.538	1.429	1.250	1.176

	0.17	150	1.333	1.176	1.176	1.111	0.909
	0.13	196	1.212	1.111	0.952	0.833	0.800
	0.1	255	1.053	1.000	0.870	0.741	0.690
	0.08	319	1.000	0.909	0.800	0.714	0.645
	0.25	102	1.667	1.429	1.333	1.053	1.000
	0.17	150	1.429	1.111	0.952	0.870	0.833
24% Al_2O_3/PDMS	0.13	196	1.176	1.111	0.870	0.800	0.690
	0.1	255	1.000	0.952	0.833	0.741	0.656
	0.08	319	0.952	0.870	0.769	0.690	0.625

Peak periodicity analysis

The shear-rate ($\dot{\boldsymbol{\gamma}}$) of the nanocomposite pastes in the process of the roll-to-roll was estimated by the equation: $\dot{\boldsymbol{\gamma}} = (\boldsymbol{U_1} - \boldsymbol{U_{21}})/\boldsymbol{d}$, where d is the rollers distance, U_1 and U_2 are the roller speed of the two rollers, respectively[13]. In this study, the $\dot{\boldsymbol{\gamma}} = \mathbf{0}$ because the $\boldsymbol{U_1} = \boldsymbol{U_2}$. The real-time viscosity (η) of the nanocomposites was based on the shear-rate estimation.

The Capillary number ($Ca=\eta U/\gamma$) was calculated for each test. The p_{spike} *vs. Ca* result is shown in Fig. S15. The result shows that the *Ca* cannot fit this fabrication very well.

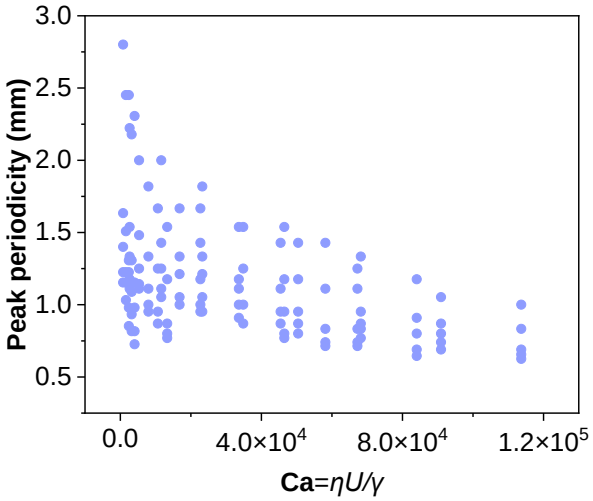

A parametric experiment of the nanocomposite pastes, Peak periodicity(p_{peak}) *vs.* Capillary number (*Ca*).

Outdoor experiment environment monitoring

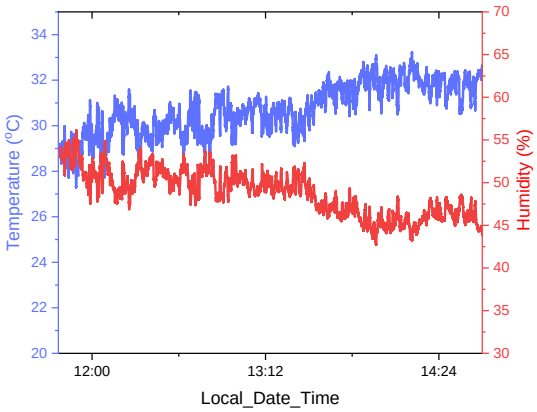

The measured temperature and relative humidity at Durham, NC on 24th, June, 2022.

Reference

1. Zhang, H. *et al.* Biologically inspired flexible photonic films for efficient passive radiative cooling. *Proc. Natl. Acad. Sci. U. S. A.* **117**, 14657–14666 (2020).
2. Mandal, J. *et al.* Hierarchically porous polymer coatings for highly efficient passive daytime radiative cooling. *Science* **362**, 315–319 (2018).
3. Li, X., Peoples, J., Yao, P. & Ruan, X. Ultrawhite BaSO4Paints and Films for Remarkable Daytime Subambient Radiative Cooling. *ACS Appl. Mater. Interfaces* **13**, 21733–21739 (2021).
4. Zhai, Y. *et al.* Scalable-manufactured randomized glass-polymer hybrid metamaterial for daytime radiative cooling. *Science* **355**, 1062–1066 (2017).
5. Li, T. *et al.* A radiative cooling structural material. *Science* **364**, 760–763 (2019).
6. Li, D. *et al.* Scalable and hierarchically designed polymer film as a selective thermal emitter for high-performance all-day radiative cooling. *Nat. Nanotechnol.* **16**, 153–158 (2021).
7. Jeong, S. Y., Tso, C. Y., Wong, Y. M., Chao, C. Y. H. & Huang, B. Daytime passive radiative cooling by ultra emissive bio-inspired polymeric surface. *Sol. Energy Mater. Sol. Cells* **206**, 110296 (2020).
8. Bohren, C. F. & Huffman, D. R. *Absorption and scattering of light by small particles*. (John Wiley & Sons, 2008).
9. Fowkes, F. M. Additivity of intermolecular forces at interfaces. I. Determination of the contribution to surface and interfacial tensions of dispersion forces in various liquids 1. *J. Phys. Chem.* **67**, 2538–2541 (1963).
10. Owens, D. K. & Wendt, R. C. Estimation of the surface free energy of polymers. *J. Appl. Polym. Sci.* **13**, 1741–1747 (1969).
11. Selvakumar, N., Barshilia, H. C. & Rajam, K. S. Effect of substrate roughness on the apparent surface free energy of sputter deposited superhydrophobic polytetrafluoroethylene coatings: A comparison of experimental data with different theoretical models. *J. Appl. Phys.* **108**, 013505 (2010).
12. Kozbial, A. *et al.* Study on the surface energy of graphene by contact angle measurements. *Langmuir* **30**, 8598–8606 (2014).
13. Park, S. H. *et al.* Bioinspired superhydrophobic surfaces, fabricated through simple and scalable roll-to-roll processing. *Sci. Rep.* **5**, 1–9 (2015).